Cellular/Molecular

Tonotopic Variation of the T-Type Ca^{2+} Current in Avian Auditory Coincidence Detector Neurons

Ryota Fukaya, Rei Yamada, and Hiroshi Kuba

Department of Cell Physiology, Graduate School of Medicine, Nagoya University, Nagoya 466-8550, Japan

Neurons in avian nucleus laminaris (NL) are binaural coincidence detectors for sound localization and are characterized by striking structural variations in dendrites and axon initial segment (AIS) according to their acoustic tuning [characteristic frequency (CF)]. T-type Ca^{2+} (CaT) channels regulate synaptic integration and firing behavior at these neuronal structures. However, whether or how CaT channels contribute to the signal processing in NL neurons is not known. In this study, we addressed this issue with whole-cell recording and two-photon Ca^{2+} imaging in brain slices of posthatch chicks of both sexes. We found that the CaT current was prominent in low-CF neurons, whereas it was almost absent in higher-CF neurons. In addition, a large Ca^{2+} transient occurred at the dendrites and the AIS of low-CF neurons, indicating a localization of CaT channels at these structures in the neurons. Because low-CF neurons have long dendrites, dendritic CaT channels may compensate for the attenuation of EPSPs at dendrites. Furthermore, the short distance of AIS from the soma may accelerate activation of axonal CaT current in the neurons and help EPSPs reach spike threshold. Indeed, the CaT current was activated by EPSPs and augmented the synaptic response and spike generation of the neurons. Notably, the CaT current was inactivated during repetitive inputs, and these augmenting effects predominated at the initial phase of synaptic activity. These results suggested that dendritic and axonal CaT channels increase the sensitivity to sound at its onset, which may expand the dynamic range for binaural computation in low-CF NL neurons.

Key words: auditory coincidence detector neurons; axon initial segment (AIS); dendrites; patch-clamp recording; T-type Ca^{2+} channels; two-photon Ca^{2+} imaging

---

Significance Statement

Neurons in nucleus laminaris are binaural coincidence detectors for sound localization. We report that T-type Ca^{2+} (CaT) current was prominent at dendrites and the axonal trigger zone in neurons tuned to low-frequency sound. Because these neurons have long dendrites and a closer trigger zone compared with those tuned to higher-frequency sound, the CaT current augmented EPSPs at dendrites and accelerated spike triggers in the neurons, implying a strategic arrangement of the current within the nucleus. This effect was limited to the onset of repetitive inputs due to progressive inactivation of CaT current. The results suggested that the CaT current increases the sensitivity to sound at its onset, which may expand the dynamic range for binaural computation of low-frequency sound.

Introduction

The interaural time difference (ITD) is a cue for sound localization and is encoded in a simple neural circuit in the brainstem of birds and mammals. Neurons in this circuit operate as coincidence detectors of excitatory signals from the two ears; the timing

of these signals differs according to the ITDs, thereby enabling the neurons to change their firing rate in a manner dependent on the ITDs. Because the signals arrive at the coincidence detectors as EPSPs and are translated into spikes, the size and kinetics of the EPSPs as well as the process of spike generation are regulated via multiple ionic mechanisms in the neurons (Kuba, 2007).

In avians, these coincidence detector neurons are found in the nucleus laminaris (NL). Importantly, NL neurons are arranged tonotopically within the nucleus, and, thus, each isofrequency region contains neurons most sensitive to sounds at a specific frequency [characteristic frequency (CF)]. Moreover, NL neurons are differentiated biophysically and morphologically along this frequency axis in chickens, and these adaptations are considered crucial for the signal processing at each isofrequency region. For example, expression of low-voltage-activated (LVA) K$^+$ chan-

nels is elevated in neurons of higher CF, and this expression narrows EPSPs and improves the coincidence detection (Kuba et al., 2005). In contrast, expression of hyperpolarization-activated cation (HCN) channels increases in lower-CF neurons (Yamada et al., 2005) and correlates with increasing dendritic length toward the lower CF (Smith and Rubel, 1979; Kuba et al., 2005). The location of the axonal trigger zone [axon initial segment (AIS)] also differs tonotopically, and approaches the soma in the lower-CF neurons (Kuba et al., 2006).

T-type Ca^{2+} (CaT) channels have been identified in dendrites and the AIS of many neurons (Christie et al., 1995; Magee and Johnston, 1995; Mouginot et al., 1997; Bender and Trussell, 2009). These channels mediate the LVA Ca^{2+} current and are characterized by a rapid and transient activation around resting membrane potentials (Perez-Reyes, 2003). Due to these characteristics, CaT channels are activated by subthreshold depolarization and contribute to the augmentation of EPSPs at dendrites, as well as the induction of burst firing and membrane potential oscillation (Huguenard, 1996; Gillessen and Alzheimer, 1997; Magee and Carruth, 1999; Cain and Snutch, 2010). CaT channels are present in NL neurons during embryonic periods (Blackmer et al., 2009), whereas tonotopic differentiations of dendrites and the AIS of the neurons have been described in older animals (Smith and Rubel, 1979; Kuba et al., 2006). However, whether the expression of CaT channels differs along the tonotopic axis and how they affect signal processing in mature NL neurons is unclear.

In this study, we examined the expression and roles of CaT channels in NL neurons of posthatch chicks, which have nearly mature auditory function, and found that CaT channels were prominent in dendrites and the AIS of low-CF NL neurons. We further revealed that activation of these channels increased the EPSP amplitude and augmented burst firing in the neurons. Because the CaT channels rapidly inactivated during a train of synaptic inputs, they likely play a major role in enhancing the responsiveness of NL to the onset of low-frequency sounds, which may expand the dynamic range for binaural computation.

Materials and Methods

Animals. Chickens of either sex between posthatch day (P)1 and P13 were used for experiments. Care for the animals was in accordance with the guidelines of Nagoya University and of the Institutional Animal Care and Use Committee of Oregon Health and Science University.

Slice preparation. Slices were prepared as described previously (Kuba et al., 2005). After decapitation under deep anesthesia with ether, the brainstem was removed and dissected in a high-glucose artificial CSF (HG-ACSF) containing the following (in mM): 75 NaCl, 2.5 KCl, 26 NaHCO₃, 1.25 NaH₂PO₄, 1 CaCl₂, 3 MgCl₂, and 100 glucose, oxygenated with 95% O₂/5% CO₂. Coronal slices with a 250 μm thickness were obtained with a vibratome (Linear Slicer Pro7, Dosaka EM). The slices were incubated in the HG-ACSF for 10–60 min at room temperature before they were transferred to a recording chamber on the stage of an upright microscope equipped with differential interference contrast optics (BX50WI, Olympus) and infrared-sensitive CCD camera (C5999, Hamamatsu Photonics). The CF of neurons in slices was estimated on the basis of a relationship between the CF and position within the nucleus (Rubel and Parks, 1975); the rostromedial one-third of the NL was defined as the high-CF region, the middle one-third as the middle-CF region, and the caudolateral one-third as the low-CF region (Fig. 1A; Kuba et al., 2005). Because the characteristics of the Ca^{2+} currents were similar between the high- and middle-CF regions, we compared these regions to the low-CF region in this study.

Electrophysiology. Whole-cell patch-clamp recordings were performed on NL neurons with Multiclamp 700B (Molecular Devices; Fig. 1B). Recording temperature was 39–41°C (body temperature of birds), except for Ca^{2+} current recording (29–31°C) and Ca^{2+} imaging (31–

33°C). A bath was perfused with an ACSF containing the following (in mM): 125 NaCl, 2.5 KCl, 26 NaHCO₃, 1.25 NaH₂PO₄, 2 CaCl₂, 1 MgCl₂, and 17 glucose, oxygenated with 95% O₂/5% CO₂; or with a TEA-based solution for Ca^{2+} current recording containing the following (in mM): 120 TEA-Cl, 10 CsCl, 5 NaCl, 1 4-aminopyridine, 2 CaCl₂, 1 MgCl₂, 10 HEPES, 15 glucose, and 0.002 tetrodotoxin (TTX; Tocris Bioscience), pH 7.4 with CsOH, oxygenated with 100% O₂. Inhibitory synaptic responses were blocked with 10 μM SR95531 (Abcam). Excitatory synaptic responses were blocked with 20 μM DNQX (6,7-dinitroquinoxaline-2,3-dione; Sigma-Aldrich), except in Figures 6 and 7. The internal solution for current-clamp recordings and Ca^{2+} imaging was a K-gluconate-based solution containing the following (in mM): 113 K-gluconate, 9–10 HEPES, 4.5 MgCl₂, 0.05–0.2 EGTA, 14 tris₂-phosphocreatine, 4 Na₂-ATP, and 0.3 tris-GTP, pH 7.2–7.3 with KOH, ~290 mOsm with sucrose; or a KCl-based solution (Fig. 1) containing the following (in mM): 160 KCl, 0.2 EGTA, and 10 HEPES-KOH, pH 7.4 with KOH, ~300 mOsm. In some experiments, KCl (27 mM) was added to the K-gluconate-based solution, while tris₂-phosphocreatine was reduced to 5 mM (Fig. 7). The internal solution for voltage-clamp recordings was a Cs-methanesulfonate-based solution containing the following (in mM): 106 Cs-methanesulfonate, 4.5 MgCl₂, 14 tris₂-phosphocreatine, 4 Na₂-ATP, 0.3 tris-GTP, 10 EGTA, 10 HEPES, and 20 TEA-Cl, pH 7.2–7.3 with CsOH, ~330 mOsm. QX-314-Br or QX-314-Cl (1 mM; Alomone) was included in the internal solution to block Na^+ currents in Figure 6A–K. At this concentration, these compounds do not impair the CaT current (Talbot and Sayer, 1996). TTA-P2 (3,5-dichloro-N-[1-(2,2-dimethyl-tetrahydro-pyran-4-ylmethyl)-4-fluoro-piperidin-4-ylmethyl]-benzamide) is a specific blocker for CaT channels (Shipe et al., 2008) and was provided from Merck. TTA-P2 was used at 1–2 μM, and the effects were evaluated at least 5 min after the perfusion. CsCl or ZD7288 (Tocris Bioscience) was added to the bath to block HCN channels (Figs. 2, 6L–P).

Pipettes were pulled from glass capillaries (GC-150TF, Harvard) with a P-97 horizontal puller (Sutter Instruments). The pipettes had a resistance of 1.5–4 MΩ when filled with the internal solutions. Electrode series resistance was compensated electronically using bridge balance for current-clamp (6–9 MΩ) by ~90%, and using series resistance compensation for voltage-clamp (4–8 MΩ) by 70–80%. The liquid junction potential (–12 mV) was corrected after the experiments. Signals were low-pass filtered at 10 kHz and digitized at 100 kHz with an NI PCIe-6251 data-acquisition board via BNC-2090A (National Instruments). Data were acquired and analyzed off-line (Axograph). A steady-state inactivation curve of the CaT current was fitted by a Boltzmann equation: $I/I_{max} = 1/(1+exp(V - V_{half})/k)$, where I is a current, I_{max} is the maximum current, V is a prepulse voltage, V_{half} is a half-inactivation voltage, and k is a slope factor. Threshold current was determined either with a 20 or 200 pA step, and threshold voltage and its latency were measured at the threshold current level. Threshold voltage was defined as the voltage corresponding to a point at which dV/dt reached 2% of the amplitude between the peak and the initial level (20–40 μs before rise), threshold latency as the time from the onset of current injection and threshold current as the minimum current required for spike induction. These spike parameters were stable over time (>5 min) in control; the shifts were -0.1 ± 0.3 mV ($p = 0.86$), -0.13 ± 0.09 ms ($p = 0.22$) and 20 ± 11 pA ($p = 0.14$), for threshold voltage, latency, and current for single-spike generation, respectively ($n = 5$), whereas the shift of threshold current for multiple-spike generation was -50 ± 50 pA ($n = 4$, $p = 0.39$). EPSCs and EPSPs were evoked with a bipolar tungsten electrode placed on the afferent axons at the medial or lateral edge of the NL (Fig. 1B). A biphasic rectangular pulse was produced by a SEN-7203 waveform generator (Nihon Kohden) and applied through a SS-202J stimulus isolator (Nihon Kohden). EPSPs were stable over time (>5 min) during a train of stimuli (10 pulses, 50 Hz) in control; the shift of amplitude was 0.7 ± 1.0 mV ($p = 0.33$) and 0.2 ± 1.1 mV ($p = 0.74$) for the first and third stimulus, respectively ($n = 3$).

Visualization of low-CF NL neurons. Neurons were visualized with AlexaFluor 594 hydrazide (10–20 μM; Life Technologies) in the pipettes. After the whole-cell recording, slices were fixed in 4% paraformaldehyde (in PBS) within 1 h at room temperature, mounted on a glass slide, dehydrated, and cleared through an ethanol-xylene series, and cover-
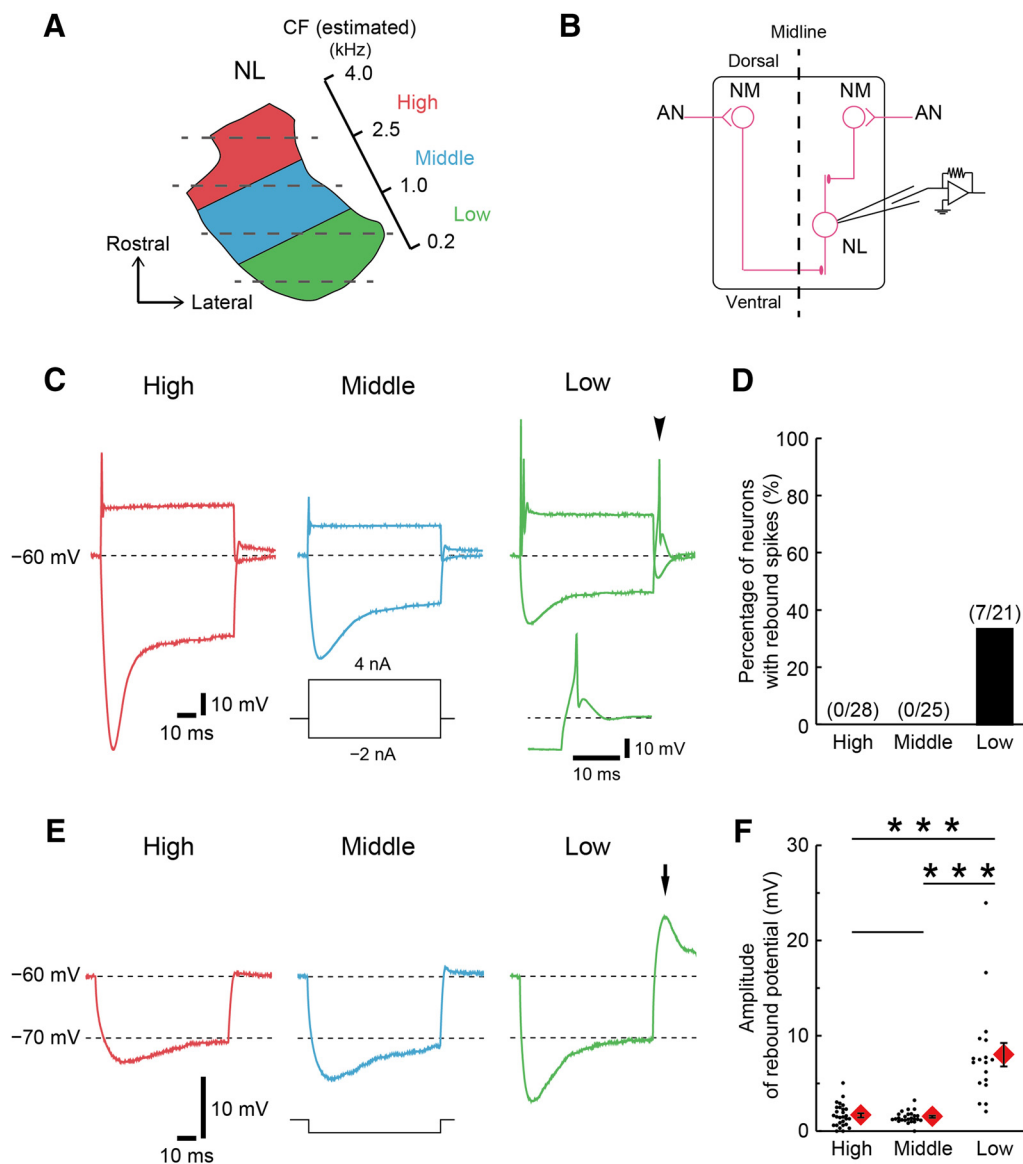
Figure 1. Rebound action potential occurred in low-CF NL neurons. ***A***, Tonotopic organization of the chicken NL. The NL was divided into three regions according to the estimated CF of the neurons (see Materials and Methods). Section lines of slices are indicated as dashed lines, and recordings were made from the caudal surface of slices. ***B***, Excitatory circuit in the avian auditory brainstem. AN, Auditory nerve; NM, nucleus magnocellularis. Left NL is displayed. ***C***, Voltage responses to rectangular currents (70 ms) of −2 and 4 nA. An action potential was elicited from a rebound depolarization in a low-CF neuron (arrowhead) and magnified in the bottom right. ***D***, Percentage of neurons that showed a rebound action potential. Columns labeled fraction of total neurons. ***E***, Voltage responses to a current injection that hyperpolarized the neuron to ∼ −70 mV. Injected current was −600 pA for high-CF, −800 pA for middle-CF, and −1600 pA for low-CF neurons. A large subthreshold rebound depolarization occurred in low-CF neuron (arrow). ***F***, Amplitude of subthreshold rebound potentials in high-CF (*n* = 28), middle-CF (*n* = 25), and low-CF neurons (*n* = 18). ***p < 0.001.

slipped. The slices were observed under a confocal microscope (FV1000, Olympus) with a 40× 0.9 NA objective. A series of images was captured at a step of 1.5 μm and Z-stacked with a maximum intensity projection (Fig. 2B), and dendritic length was measured with ImageJ (see Results).

Calcium imaging. Ca^{2+} imaging was performed as described by Bender and Trussell (2009). A Ti:sapphire-pulsed laser (Chameleon Ultra II, Coherent) powered a Prairie Technologies Ultima two-photon imaging system. The laser intensity was modulated with a Pockels cell (350–80 LA, Conoptics). The laser was tuned to 810 nm. The pipette solution included Fluo-5F (250 μM, Ca^{2+} indicator; Life Technologies, green) and AlexaFluor 594 (20 μM, volume marker; red), whereas EGTA was omitted. Epi- and trans-fluorescence signals were captured through a 60× 0.9-NA objective and a 1.4-NA oil-immersion condenser (Olympus). Fluorescence was split into red and green channels using dichroic mirrors and bandpass filters (epi: 575 DCXR, HQ525/70, HQ607/45; trans: T560LPXR, ET510/80, ET620/60; Chroma) and then focused on photomultiplier tubes (H8224 or R9110, Hamamatsu Photonics). Data were collected in the line-scan mode at 2.2 ms/line, including mirror flyback.

Data are presented as averages of 10–20 events per site and expressed as $\Delta(G/R)/(G/R)_{\text{max}} \times 100$, where $(G/R)_{\text{max}}$ is the maximal fluorescence measured at 2 mM Ca^{2+} (Yasuda et al., 2004). Peaks of Ca^{2+} transients were calculated from exponential fits of the fluorescence decay following stimulus offset. Dendrites were scanned within the proximal and distal thirds of the dendrites, while axons were scanned along the axons using a 5 μm step.

Statistics. Values are presented as the mean ± SEM. A paired or unpaired Student's *t* test was used, and the equality of variances was checked with an *F* test. The level of statistical significance was set at 0.05.

Results

Rebound depolarization in low-CF NL neurons

Voltage responses to rectangular currents were qualitatively similar within the NL (Fig. 1C); neurons showed one or a few spikes at the onset of depolarization (4 nA) and a voltage sag during hyperpolarization (−2 nA), regardless of the CF. However, the responses varied quantitatively according to CF; spikes were the
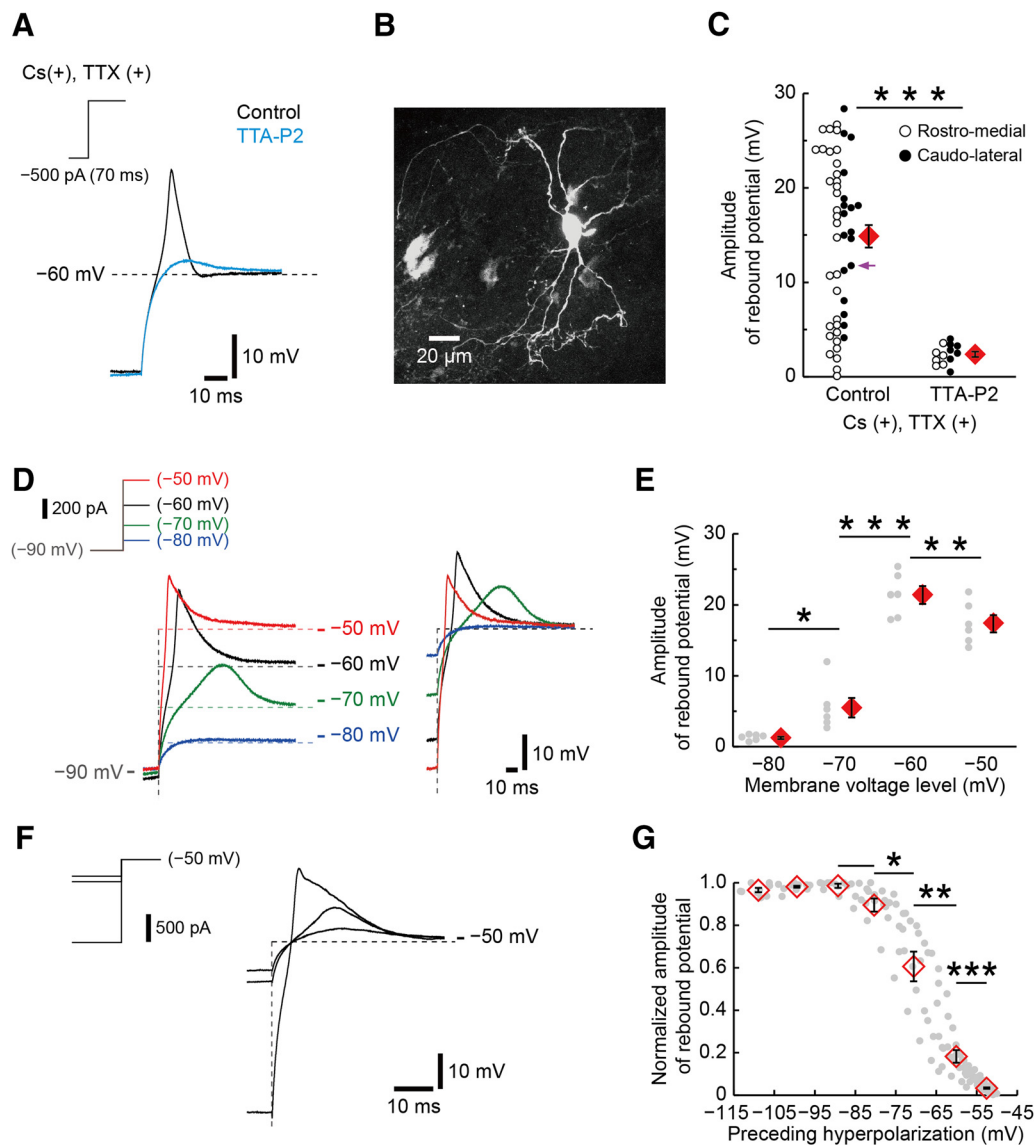
Figure 2. CaT current mediated rebound potential in low-CF neurons. ***A***, Voltage responses to a −500-pA current (70 ms) under HCN current (5–10 mM CsCl) and Na⁺ current (1–2 μM TTX) blockade in low-CF neurons. The rebound potential appeared at −60 mV following hyperpolarization ∼−90 mV (black), which was diminished by TTA-P2, a blocker of the CaT current (blue). ***B***, Confocal image of a neuron that exhibited a rebound potential. ***C***, Amplitudes in ***A*** were plotted for control (n = 50) and with TTA-P2 (n = 13). Values from rostromedial (n = 32 in control; n = 6 in TTA-P2) and caudolateral halves of low-CF region (n = 18 in control; n = 7 in TTA-P2) are shown in open and filled symbols, respectively. A value from a P13 animal is indicated by a purple arrow. ***D***, ***E***, Voltage dependence of the activation of the rebound potential. Membrane was held at −80, −70, −60, and −50 mV, and a rebound was elicited by a preceding hyperpolarization (70 ms) of −90 mV (left). Traces were aligned at a holding voltage to compare the rebound depolarization height (right; ***D***). The rebound height was plotted against the holding voltage (n = 6, for each voltage; ***E***). ***F***, ***G***, Voltage dependence of the inactivation of rebound potentials determined by recording at −50 mV with various levels of preceding hyperpolarization (70 ms; ***F***). The responses in ***F*** were induced by currents of −300, −400, and −1500 pA. The amplitudes were normalized to the maximum in individual neurons and plotted against the hyperpolarization level (***G***, gray dots; n = 8). The normalized values were averaged in a 10 mV bin between −115 and −55 mV, and a 5 mV bin >−55 mV (diamonds). The SEM of the steady-state voltage was <0.8 mV. Note that the rebound appeared even with a preceding hyperpolarization ∼−60 mV. *p < 0.05, **p < 0.01, ***p < 0.001.

largest, and the level of hyperpolarization was the smallest in low-CF neurons, suggestive of the lowest expression of LVA K⁺ channels and the highest expression of Na⁺ channels and HCN channels in these neurons (Kuba et al., 2005, 2006; Yamada et al., 2005). Notably, the responses also differed in a rebound depolarization following the hyperpolarization. The rebound potential was prominent in the low-CF neurons and generated spikes in 7 of 21 neurons (Fig. 1C,D). Indeed, when the rebound potential was maintained at subthreshold by setting a preceding hyperpolarization ∼−70 mV (between −1.8 and −0.2 nA), the amplitude was approximately five times larger in low-CF neurons than in high-CF and middle-CF neurons (Fig. 1E,F). The rebound potential decreased but persisted even after blockade of Na⁺

channels and HCN channels; the amplitude was 10.8 ± 1.8 mV (n = 14) and 5.4 ± 1.1 mV (n = 6) at −60 mV after a preceding pulse ∼−75 mV without and with the blockades, respectively (p = 0.016; data not shown). More importantly, further application of a specific blocker for CaT channels (TTA-P2) nearly eliminated the rebound potential (Fig. 2A,C), indicating that the rebound is substantially generated by CaT channels. Consistently, neurons exhibiting the rebound possessed a few, long primary dendrites (>50 μm; 103.2 ± 9.4 μm, 17 neurons; Fig. 2B), which are characteristic of NL neurons in the low-CF region (Smith and Rubel, 1979; Kuba et al., 2005). Some neurons showed a smaller rebound (<5 mV, 9 of 50 neurons), and these neurons were preferentially located in the rostromedial half of the low-CF re-
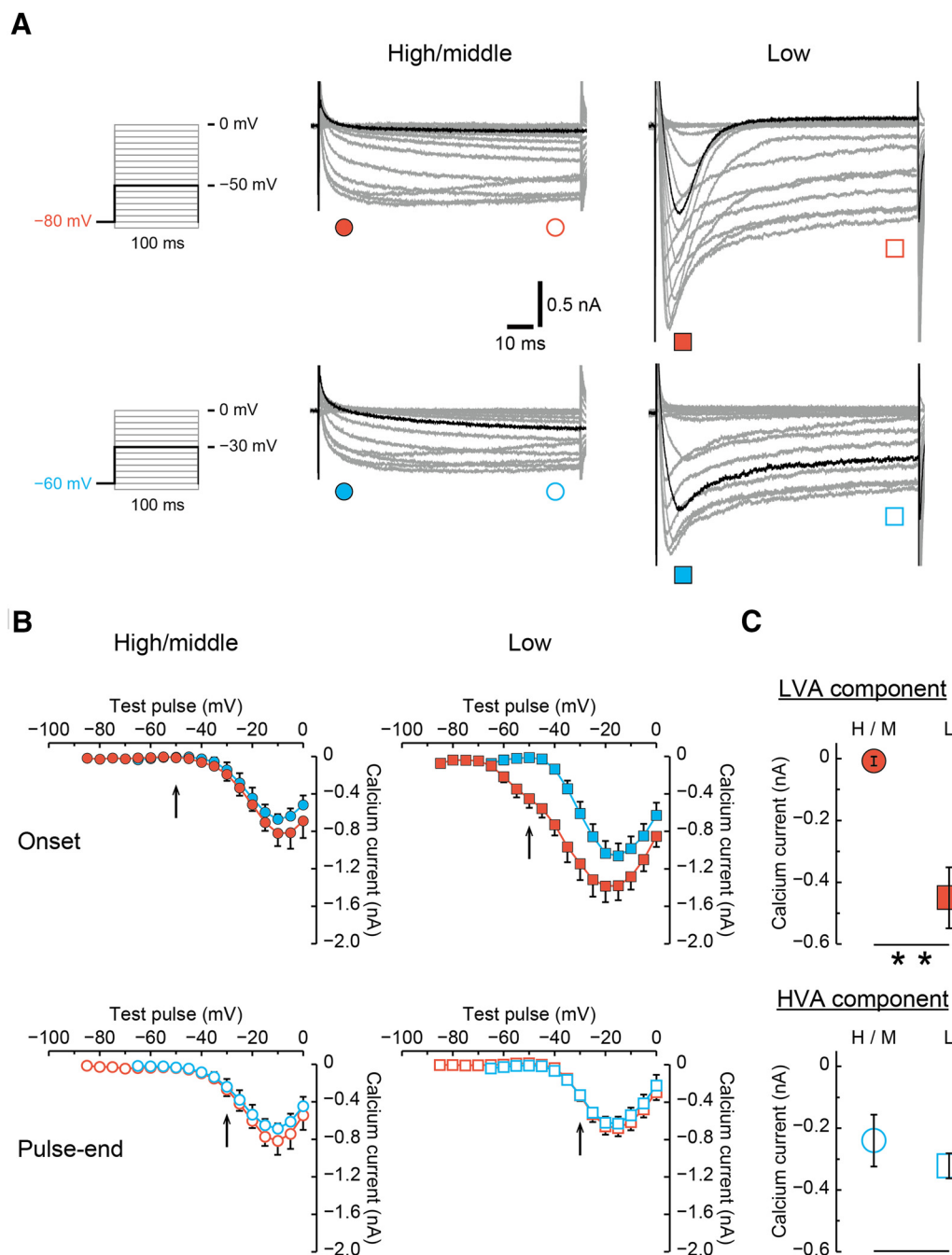
Figure 3. CaT current was large in low-CF neurons. **A**, Ca²⁺ current in NL neurons. Currents were recorded in high/middle-CF (middle) and low-CF (right) neurons at a holding voltage of −80 mV (top) and −60 mV (bottom). Voltage pulses (100 ms) were varied from −85 to 0 mV for −80 mV and from −65 to 0 mV for −60 mV, with a 5 mV step (left). In **A**–**C**, Filled symbols for the onset and open symbols for the pulse-end of the trace. **B**, I–V relationships at the onset (top) and pulse-end (bottom) for the holding voltage of −80 mV (red) and −60 mV (blue). The maximal current amplitudes were measured within 20 ms from the onset or pulse-end. Left, High/middle-CF (n = 4); right, low-CF neurons (n = 9). **C**, LVA (top) and HVA (bottom) components. LVA and HVA components were calculated from the red filled symbols at −50 mV and from the blue open symbols at −30 mV, respectively (**A**, black traces; **B**, arrows; see Results). H/M, high/middle-CF; L, low-CF. **p < 0.01.

gion (8 of 9 neurons; Fig. 2C, open symbols). Nevertheless, the average amplitude did not differ within the region; it was 14.4 ± 1.6 mV (n = 32) and 15.8 ± 1.7 mV (n = 18) for the rostromedial and caudolateral halves, respectively (p = 0.59).

The voltage dependence of the rebound potential activation and inactivation was compatible with those of CaT channels, which activate and inactivate at potentials near the resting potential of neurons (Perez-Reyes, 2003). When the rebound potential was recorded at various levels of holding voltage, it was apparent above −70 mV, and its amplitude increased with depolarization,

reaching a peak at −60 mV (Fig. 2D,E). In contrast, when the rebound potential was recorded at −50 mV with various levels of a hyperpolarizing prepulse, it appeared even with a prepulse of ∼−60 mV and reached a maximum at −90 mV (Fig. 2F,G). These results indicated that CaT channels could be substantially activated at the resting potential in low-CF NL neurons.

LVA CaT current was prominent in low-CF NL neurons
The tonotopic variation of CaT channels was further explored by recording Ca²⁺ currents from the soma of high/middle-CF and

low-CF neurons under voltage-clamp (Fig. 3). Two levels of holding voltages (−80 mV and −60 mV) were used to dissect the LVA CaT current and high-voltage-activated (HVA) Ca²⁺ current (Blackmer et al., 2009). At a holding voltage of −80 mV, the test pulses induced a sustained inward current in high/middle-CF neurons and both transient and sustained inward currents in low-CF neurons (Fig. 3A, top). In contrast, at a holding voltage of −60 mV, the sustained inward current remained in both neurons, whereas the transient current was substantially smaller in the low-CF neurons (Fig. 3A, bottom). The transient current corresponded to an LVA CaT current, as it appeared near the resting potential ($\sim$−65 mV; Fig. 3B, top right, filled red squares). However, the sustained current appeared at potentials above −40 mV (Fig. 3B, bottom, open symbols) and was activated with a rather slow time course, compatible with the properties of an HVA Ca²⁺ current (Blackmer et al., 2009). Thus, we measured the LVA CaT component as the onset current at −50 mV (Fig. 3B, top, arrows) with a holding voltage of −80 mV and the HVA component as the pulse-end current at −30 mV (Fig. 3B, bottom, arrows) with a holding voltage of −60 mV (Fig. 3C). Thus, the LVA component was significantly larger in low-CF neurons than in high/middle-CF neurons ($p = 0.0022$; Fig. 3C, top), whereas the HVA component did not differ between the neurons ($p = 0.33$; Fig. 3C, bottom). These results indicated that the LVA CaT current is a specialization of low-CF neurons, whereas the HVA Ca²⁺ current is found throughout the NL.

We isolated the LVA CaT current in low-CF neurons by subtracting the Ca²⁺ current with a −60 mV holding voltage from that with a −80 mV holding voltage (Fig. 4A,B). The isolated currents were activated and inactivated rapidly upon depolarization above −65 mV. The time constants of these currents were calculated with m³h fitting (Coulter et al., 1989) and were 2.1 ± 0.3 ms ($n = 9$) and 12.7 ± 1.4 ms ($n = 9$) at −60 mV for activation (m) and inactivation (h), respectively (Fig. 4C,D), which corresponds to $\sim$0.5 and $\sim$3 ms at the body temperature of birds (40°C) with a Q10 of 4 (Blackmer et al., 2009).

The voltage dependence of inactivation of the CaT current was analyzed with a double-pulse protocol, where a prepulse of 100 ms between −100 and −50 mV (5 mV increment) preceded a −50 mV test pulse (Fig. 4E). A transient current appeared when the prepulse was below −60 mV and saturated at $\sim$−100 mV. The plot of the normalized amplitude (I/I_{max}) was fitted to a Boltzmann equation (see Materials and Methods), showing an inactivation V_{half} of -75.7 ± 1.3 mV ($n = 3$; Fig. 4F). Although the value was more hyperpolarized than in previous reports (V_{half} of −64.1 mV; Blackmer et al., 2009), this could be related to the long dendrites of posthatch low-CF neurons (Smith and Rubel, 1979), which can cause a negative shift in the inactivation V_{half} because of the limitation of space clamp. The time dependence of the recovery from inactivation was evaluated by changing the duration of the prepulse (−100 mV, 1–500 ms) at a holding voltage of −50 mV (Fig. 4G), showing that the CaT current recovered from inactivation with a prolongation of the prepulse with a time constant of 87.1 ± 9.9 ms ($n = 6$; Fig. 4H). This value corresponds to $\sim$20 ms at 40°C (Blackmer et al., 2009).

Subcellular localization of Ca²⁺ transients in NL neurons

We examined the Ca²⁺ transients associated with spikes in dendrites and an axon of NL neurons in high/middle-CF and low-CF regions by using a two-photon microscope (see Materials and Methods). We evoked spikes by injecting a pulse train (1 ms, 2 nA, 6 pulses at 100 Hz) and made line scans at the corresponding regions in the NL neurons (Fig. 5A,B). Ca²⁺ transients ($\Delta G/R$)
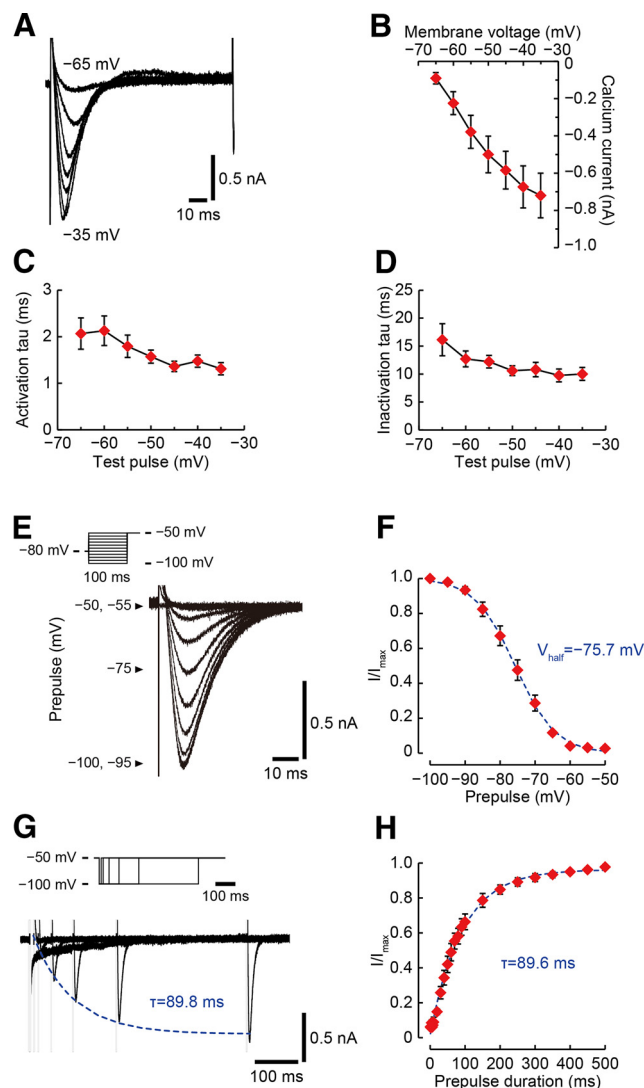

Figure 4. Biophysical properties of the CaT current in low-CF neurons. **A, B**, Voltage dependence of the activation of the LVA component in low-CF neurons. LVA components were isolated as tail currents by subtracting the Ca²⁺ current with a −60 mV prepulse (Fig. 3A, bottom right) from that with a −80 mV prepulse (Fig. 3A, top right; **A**). The peak amplitudes of the isolated currents are plotted in **B** ($n = 9$). **C, D**, Activation and inactivation tau of the LVA components from the m³h fitting in **A. E, F**, Voltage dependence of the inactivation of the LVA component. The Ca²⁺ current was recorded at −50 mV with various levels (from −100 to −50 mV) of a prepulse (100 ms; **E**). I/I_{max} was plotted against the prepulse voltage and fitted to the Boltzmann equation (**F**; $n = 3$). **F–H**, The fitted curve is shown as a dashed line. **G, H**, Time course of recovery from the inactivation of the LVA component. The Ca²⁺ current was recorded at −50 mV with various durations (from 1 to 500 ms) of the prepulse (−100 mV). The currents at a prepulse duration of 10, 20, 50, 100, 200, and 500 ms are shown, and the capacitive artifacts are concealed in **G**. Average I/I_{max} was plotted against the prepulse duration (**H**; $n = 6$). A single exponential function was used for fitting in **G** and **H**.

were small or not apparent at both proximal and distal dendrites in high/middle-CF neurons, whereas the signals were three to five times larger at both locations in low-CF neurons (Fig. 5C; see Materials and Methods).

We also observed Ca²⁺ transients in the axon regardless of the CF region (Fig. 5B, bottom, D). The maximum response occurred at a more proximal location in low-CF neurons than in higher-CF neurons (Fig. 5E); the location was 36 ± 4 μm away from the soma in high/middle-CF and 7 ± 1 μm in low-CF neurons ($n = 5$, $p = 0.00067$), presumably reflecting the location of the AIS (Kuba et al., 2006). These results may support the
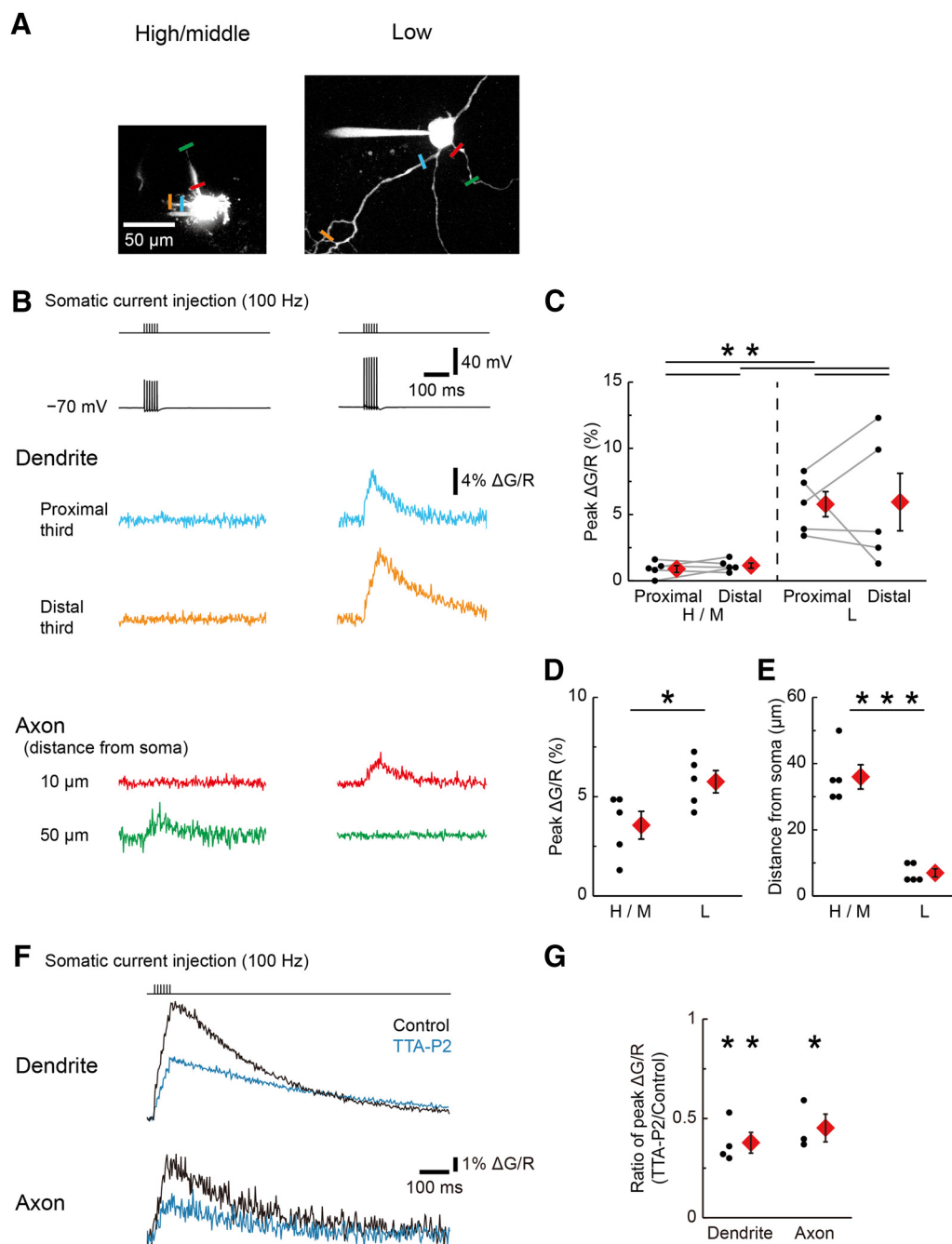
Figure 5. Dendritic Ca^{2+} transient was prominent in low-CF neurons. **A**, High/middle-CF (left) and low-CF (right) neurons visualized with AlexaFluor 594. **B**, Simultaneous current-clamp recording and Ca^{2+} measurement (Fluo-5F, $\Delta G/R$). Spikes in response to a train of 6 pulses (100 Hz; see Results) were recorded at the soma (top), and Ca^{2+} transients were imaged at locations indicated by lines in **A**; proximal (blue) and distal (orange) thirds of dendrites (middle), 10 (red), and 50 μm (green) away from the soma on the axon (bottom; see Materials and Methods). **C, D**, Peak $\Delta G/R$ at proximal and distal dendrites (**C**) and axon (**D**). Maximum peak $\Delta G/R$ in the axon was plotted. **E**, Location that provided the maximum $\Delta G/R$ in the axon. In **C–E**, H/M, high/middle-CF ($n = 5$); L, low-CF neurons ($n = 5$). **F**, Ca^{2+} transients before (black) and after TTA-P2 (blue) at dendrites (top) and axon (bottom) in low-CF neurons. **G**, Relative peak $\Delta G/R$ at dendrites ($n = 4$) and the axon ($n = 3$). *$p < 0.05$, **$p < 0.01$, ***$p < 0.001$.

larger Ca^{2+} current in the low-CF neurons (Fig. 3). Nevertheless, Ca^{2+} transients are influenced by multiple factors, including surface-to-volume ratio and extent of depolarization at the locations as well as Ca^{2+} entry, and therefore, it is difficult to relate them directly to the density of Ca^{2+} channels.

Importantly, depolarizing the membrane at rest from −70 to −60 mV decreased Ca^{2+} transients in response to the spikes by half in low-CF neurons, 53 ± 12% ($n = 3$) in the dendrites and 64 ± 8% ($n = 3$) in the axon. Moreover, TTA-P2 suppressed the

Ca^{2+} transients by 60% at these locations (Fig. 5 F, G), suggesting that the CaT current contributed to the Ca^{2+} transients in low-CF neurons. These results indicated that CaT channels are expressed in dendrites and the axon in the low-CF NL neurons.

CaT current transiently augmented EPSPs in low-CF NL neurons

We next examined how the dendritic CaT channels affect unilateral synaptic responses in low-CF NL neurons. In these experiments,

postsynaptic Na$^+$ channels were blocked with intracellular QX-314 (1 mM; Fig. 6A–K; see Materials and Methods). Bath application of TTA-P2 reduced the EPSP amplitude by 34%, whereas it did not affect the amplitude of EPSCs (Fig. 6A–D). TTA-P2 slightly distorted the decay phase of EPSCs (Fig. 6C, arrow; 3 of 5 cells), suggesting that CaT current was activated during EPSCs due to the limitation of space clamp at dendrites of the neurons. Nevertheless, TTA-P2 affected neither the rise time nor the half-width of the EPSCs (n = 5); the half-width was 3.41 ± 0.47 and 2.68 ± 0.41 ms (p = 0.10), whereas the 10–90% rise time was 0.44 ± 0.10 and 0.46 ± 0.11 ms (p = 0.45) before and after the drug, respectively. The results indicated that the CaT current was activated by synaptic depolarization and augmented the response in the low-CF neurons. Consistent with this interpretation, TTA-P2 shortened the latency of the peak of the EPSP (8 of 8 neurons), with little effect on its rising rate (Fig. 6G,H). Surprisingly, TTA-P2 did not substantially elongate the half-widths of the EPSPs (Fig. 6E,F). This may be because the LVA K$^+$ current was activated and counterbalanced the prolonged activation of the CaT current during the EPSP (Kuba et al., 2003).

The effect of the CaT current on the EPSP was dependent on the EPSP amplitude (Fig. 6I,J). With an elevation in the stimulus intensity, the EPSP amplitude increased in both the control and TTA-P2 conditions, but the extent was smaller for TTA-P2 (Fig. 6J). When the effects of TTA-P2 were measured as a reduction in EPSP amplitude (ΔV; see figure legends), the reduction became apparent when the EPSP amplitude was between 5 mV (S$_5$) and 15 mV (S$_{15}$; Fig. 6K). This observation was consistent with the voltage range for activation of the CaT current in the neurons (∼−65 mV; Figs. 3, 4). However, a further increase in the EPSP amplitude did not enhance the effects of TTA-P2 (S$_{20}$). This reduction in the contribution of CaT channels for large EPSPs probably reflects the activation of K$^+$ channels at more depolarized potentials.

NL neurons receive sequential synaptic inputs at a rate similar to their CF during ongoing sounds (Köppl and Carr, 2008; Funabiki et al., 2011). We therefore examined the effect of TTA-P2 on EPSPs during a train of 10 stimuli at 50 Hz in the low-CF neurons (Fig. 6L). In control conditions, the train of stimuli caused synaptic depression; the amplitude of the EPSPs declined and reached a steady level of ∼5 mV by the third stimulus. After application of TTA-P2, the EPSPs were suppressed, but the effect was limited to the first stimulus (10.3 ± 2.0 mV in control and 8.3 ± 1.7 mV in TTA-P2; n = 4, p = 0.014; Fig. 6L,M). A similar tendency was observed at 200 Hz, within the range of low-frequency sound in chickens; the amplitude was 9.4 ± 1.2 and 7.2 ± 1.3 mV at the first stimulus (p = 0.0013), whereas it was 6.5 ± 0.5 and 6.7 ± 0.7 mV at the second stimulus (p = 0.87), before and after TTA-P2, respectively (n = 3).

We then applied TTA-P2 while injecting a 50 Hz sine wave current whose amplitude was constant for a given trial (375 ± 48 pA, n = 4; Fig. 6N,O). The current caused phasic depolarizations of a size comparable to the EPSP at the first synaptic stimulus (Fig. 6L,M). Similarly, TTA-P2 reduced the amplitude at the first stimulus (13.1 ± 0.7 mV in control and 10.0 ± 0.4 mV in TTA-P2; n = 4, p = 0.0062) and did not affect the later responses. At higher frequencies, however, the effect was not limited to the first stimulus (Fig. 6P), suggesting that the lack of TTA-P2 effects on the later EPSPs would be at least in part due to the reduction of EPSP amplitude by the synaptic depression; the maximum reduction was 2.6 ± 0.6 mV (p = 0.0089) at around the third (2.8 ± 1.3) stimulus for 400 Hz (n = 5), whereas 2.3 ± 0.7 mV (p = 0.033) at around the second (2.0 ± 0.8) stimulus for 200 Hz

(n = 5). Nevertheless, the maximum effects still occurred within 20 ms after the beginning of current injection, confirming that the CaT current was activated primarily at the onset of the repetitive inputs, likely reflecting progressive inactivation of the CaT current during the train of stimuli.

Effects of the CaT current on spike generation in low-CF NL neurons

Figure 7A shows the effects of TTA-P2 on spike generation in response to synaptic inputs (5 inputs at 50 Hz; Fig. 7A, see Materials and Methods). Spikes were elicited from the first EPSP with a probability of 0.3–0.8 in the absence of the drug (top left), and they were completely abolished after application of TTA-P2 (top right) with little effect on the EPSCs (bottom), confirming that CaT current augmented spike generation by boosting EPSPs in low-CF neurons; the probability was 0.56 ± 0.10 and 0.05 ± 0.05 before and after TTA-P2, respectively (n = 4, p = 0.016; Fig. 7B).

We then induced a spike by injecting a current into the soma (Fig. 7C–E). TTA-P2 changed neither the threshold voltage nor its latency; the shifts were −1.2 ± 0.8 mV (n = 7, p = 0.22) for the threshold voltage and −0.14 ± 0.16 ms (n = 7, p = 0.42) for the latency. In addition, TTA-P2 did not affect the threshold current for generating a single spike (104 ± 7%, n = 5, p = 0.62; Fig. 7F). This contrasted with the effect of the CaT current on spike generation from EPSPs (Fig. 7A), highlighting the importance of a dendritic CaT current in the enhancement of spike generation. Nevertheless, TTA-P2 still increased the threshold current for generating the second spike during the somatic current injection (123 ± 7%, n = 7, p = 0.017; Fig. 7G,H), and the increase was augmented after raising the input resistance via blockade of HCN channels with Cs$^+$ (161 ± 35%, n = 5, p = 0.0046; Fig. 7I,J). The input resistance was 17.2 ± 2.2 MΩ (n = 11) and 38.5 ± 4.8 MΩ (n = 6) without and with Cs$^+$, respectively (p = 0.00035). These results suggested that the CaT current contributed to the induction of spike bursts at the axon in the low-CF neurons.

Discussion

In this study, we showed that the CaT current was present in dendrites and the AIS of low-CF NL neurons in posthatch chicks and contributed to augmenting synaptic potentials and promoting spike generation in the neurons. Because CaT channels are subject to inactivation with depolarization, this effect was restricted to the initial phase during sequential inputs. These findings suggest that the CaT current increases the responsiveness of low-CF NL neurons at sound onset, which may increase the sensitivity of these neurons to acoustic stimuli.

Developmental changes of the CaT current in NL neurons

Although the CaT current was found in all NL neurons of late-stage embryos (E14–E18; Blackmer et al., 2009), it was restricted to the low-CF region (probably <500 Hz) in posthatch animals. This implies that CaT channels in higher-CF regions were eliminated during development, as reported for other types of neurons (Chameau et al., 1999; Martin-Caraballo and Greer, 2001; Levic and Dulon, 2012). However, this elimination is unlikely to also occur in low-CF neurons of still older chicks. The CaT current mediated the rebound depolarization even in an animal older than P10 (Fig. 2C, purple arrow), and the amplitude of CaT current did not differ between embryos (Blackmer et al., 2009) and posthatch animals (Fig. 4; ∼0.8 nA at −35 mV). Thus, the CaT current is probably maintained in low-CF NL neurons and may play substantial roles in signal processing of these neurons. Notably, the HVA Ca^{2+} current decreased during development in
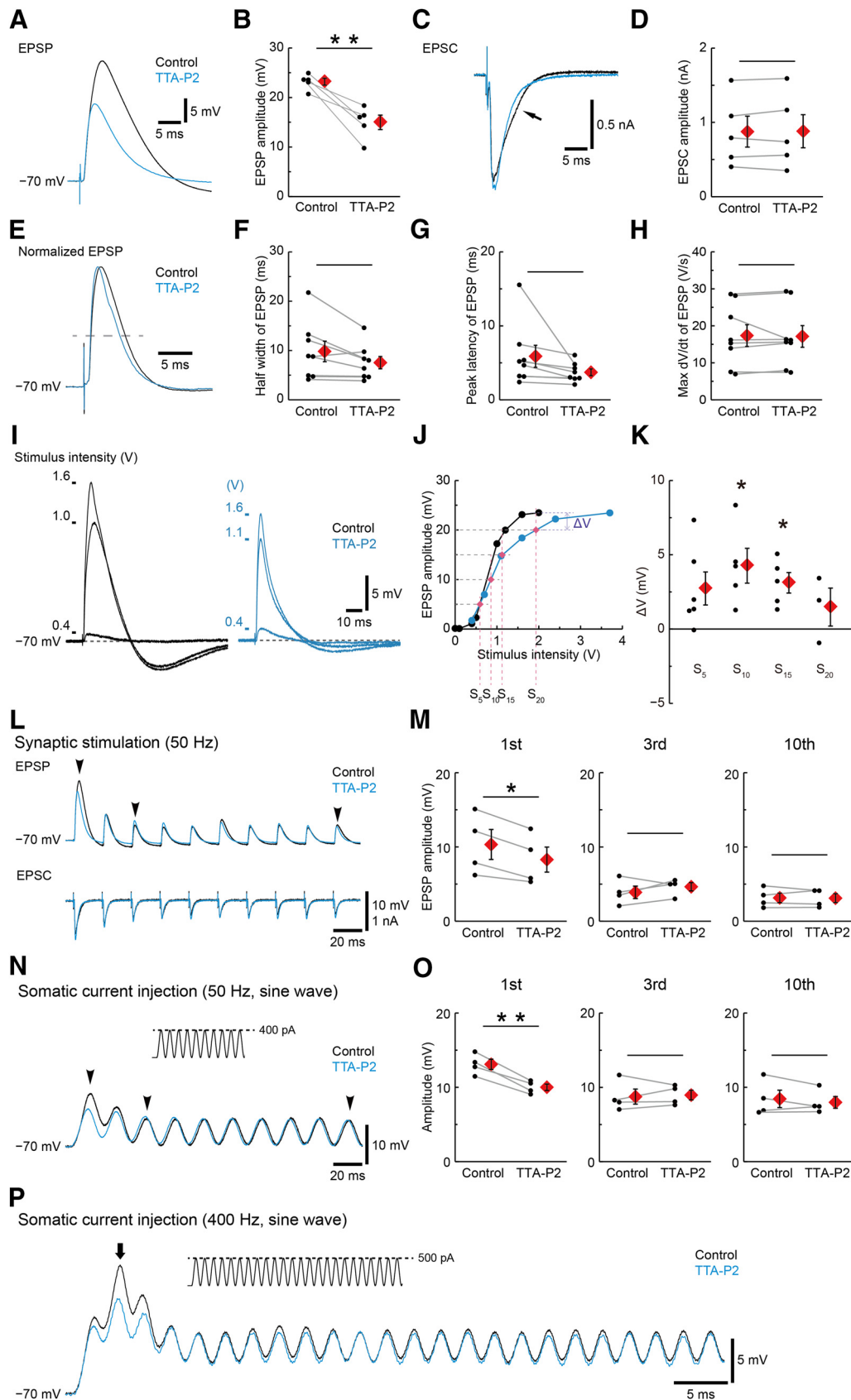
Figure 6. Effects of the CaT current on synaptic depolarization in low-CF neurons. **A–D**, EPSPs (**A**) and EPSCs (**C**) were recorded at −70 mV before (black) and after TTA-P2 (blue). The arrow in **C** indicates the distortion of the EPSC in control conditions (see Results). In **A–K**, QX-314 (1 mM) was included in the recording pipette. Amplitude of EPSPs (**B**) and EPSCs (**D**; $n = 5$). **E–H**, EPSPs before (black) and after TTA-P2 (blue) were normalized. The dashed line indicates the half amplitude. Half-width (**F**), peak latency (**G**), and maximum dV/dt (**H**) of EPSPs ($n = 8$). **I**, EPSPs elicited by three different intensities before (left) and after TTA-P2 (right). **J**, EPSP amplitude in **E** was plotted against the stimulus intensity. ΔV was calculated as a subtraction of the EPSP amplitude after TTA-P2 from that before TTA-P2. **K**, ΔV at stimulus intensities corresponding to EPSP amplitudes of 5 mV (S_5; $n = 6$), 10 mV (S_{10}; $n = 5$), 15 mV (S_{15}; $n = 5$), and (*Figure legend continues.*)
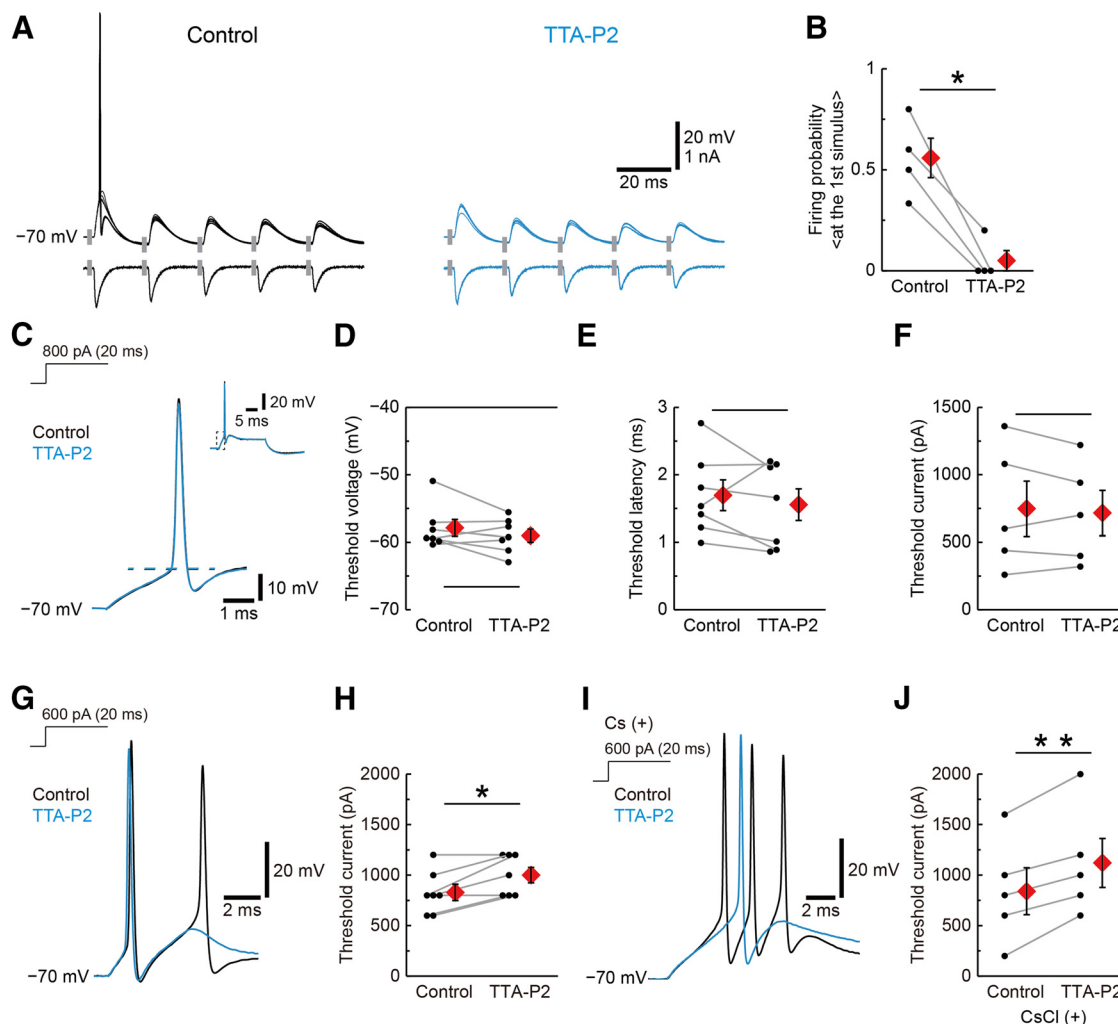
Figure 7. Effects of the CaT current on spike generation in low-CF neurons. *A*, EPSPs (top) and EPSCs (bottom) during a train of 5 stimuli (50 Hz). Ten and five traces were superimposed for before (left) and after TTA-P2 (right). Spikes were generated from the first EPSP in control, which were blocked after application of TTA-P2. Stimulus artifacts were concealed. *B*, Firing probability at the first stimulus before and after TTA-P2 ($n = 4$). TTA-P2 affected the amplitudes of neither the EPSCs nor the EPSPs in the later phase. *C–E*, Voltage responses to the threshold current (20 ms) for single-spike generation. In *C–J*, before (black) and after TTA-P2 (blue). Dashed lines indicate the threshold voltage. The voltage responses were used to measure the threshold voltage (*D*) and its latency (*E*; $n = 7$). *F*, Threshold current for single-spike generation determined with a 20-pA step ($n = 5$). *G, I*, Voltage responses to the threshold current for multiple-spike generation in control without (*G*) and with CsCl (2 mM; *I*). Note that TTA-P2 suppressed the generation of multiple spikes at the currents. *H, J*, Threshold current for multiple-spike generation before and after TTA-P2 without (*H*; $n = 7$) and with CsCl (*J*; $n = 5$). *$p < 0.05$, **$p < 0.01$.

NL neurons and was similar across the tonotopic regions (Fig. 3*B*, bottom; Blackmer et al., 2009). This uniform expression is in contrast to the CF-specific decline of the CaT current and further highlights the potential significance of the CaT current in the low-CF neurons.

Dendritic and axonal CaT current in low-CF NL neurons
Imaging results showed that CaT channels are present in both dendrites and the AIS in low-CF NL neurons (Fig. 5). TTA-P2

(*Figure legend continued.*) 20 mV (S₂₀; $n = 3$) with TTA-P2. *L*, Train of subthreshold EPSPs (50 Hz; top) and EPSCs (bottom) from a neuron before (black) and after TTA-P2 (blue). *M*, Amplitude of the EPSP at the first, third, and 10th stimulus (*L*, arrowheads; $n = 4$). CsCl (2 mM) or ZD7288 (20 μM) was added to the bath in *L–P*. *N*, Voltage responses to a somatic sinusoidal current injection (400 pA, 50 Hz) before (black) and after TTA-P2 (blue). *O*, Peak amplitude at the first, third and 10th stimulus (*N*, arrowheads; $n = 4$). *P*, Voltage responses to a somatic sinusoidal current injection (500 pA, 400 Hz) before (black) and after TTA-P2 (blue). Arrow indicates the phase showing the maximum decrement by TTA-P2. *$p < 0.05$, **$p < 0.01$.

diminished the EPSP amplitude and reduced the probability of spike generation in the neurons (Figs. 6, 7). In contrast, TTA-P2 suppressed somatic depolarization during current injection but did not change the threshold current for generating a spike (Figs. 6, 7). Thus, EPSPs activated CaT channels and augmented spike generation more efficiently than somatic depolarization. This is reasonable because CaT channels are abundant in the dendrites (Fig. 5), and excitatory synaptic terminals are formed predominantly at this location in neurons (Parks et al., 1983). Importantly, however, when multiple spikes were induced during somatic current injection, TTA-P2 elevated the threshold current for the second spike, suggesting that CaT channels at the AIS could still promote spike bursts in the neurons, which is compatible with observations in mammalian auditory neurons (Bender and Trussell, 2009). Notably, the AIS of NL neurons is differentiated in its location and length along the tonotopic axis (Kuba et al., 2006), which is shaped in part by afferent inputs (Kuba et al., 2014). Intracellular Ca²⁺ is crucial for structural reorganization of the AIS (Evans et al., 2013). Therefore, the CaT channels at the

AIS may also contribute to the reorganization and/or the maintenance of the AIS structure in NL neurons.

Effects of the CaT current on signal processing of low-CF NL neurons

We showed that CaT channels amplified EPSPs specifically in low-CF NL neurons of posthatch animals (Fig. 6). Because these neurons have long dendrites, this amplification may compensate for the attenuation of EPSPs that are initiated toward the ends of dendrites. Interestingly, although the progressive inactivation of CaT channels restricted this amplification to EPSPs only at the beginning of a train of stimuli (Chemin et al., 2002; Uebachs et al., 2006), the amplification may nevertheless play a role in the encoding of ITDs. When a sound is weak, NL neurons receive small EPSPs from both sides of the nucleus magnocellularis. Summation of these EPSPs is the most efficient for coincident bilateral inputs, whereas CaT current amplifies subthreshold EPSPs with a substantial size (>5 mV; Fig. 6J,K). Therefore, this amplification may help the coincident EPSPs to reach spike threshold, thereby expanding the dynamic range for ITD detection. When a sound is stronger, the CaT current would promote the generation of multiple spikes, particularly for coincident EPSPs rather than for out-of-phase EPSPs (Figs. 7G–J, 6J, K), which would further expand the dynamic range. In support, doublet spikes in low-CF NL neurons *in vivo* preferentially occur at the onset of in-phase inputs during strong sound stimuli (Nishino et al., 2008). Thus, the CaT current would contribute to improving ITD detection through amplifying the EPSP amplitude and augmenting spike generation particularly at the onset of sound inputs in the low-CF NL neurons. It is interesting to note that the onset of sound has been revealed to be the most important for humans to discriminate ITDs for sound frequencies >200 Hz (Brown and Stecker, 2010; Diedesch and Stecker, 2015), which corresponds to the lowest CFs that are present in the chicken NL (Rubel and Parks, 1975).

CaT channels induced a depolarizing rebound that followed the termination of a hyperpolarizing current, which triggered action potentials in some neurons (Figs. 1, 2). Such an excitation following a hyperpolarization has been termed post-inhibitory rebound and may be a mechanism for encoding sound termination and/or rhythms in the auditory system (inferior colliculus: Casseday et al., 1994; Faure et al., 2003; paraolivary nucleus: Felix et al., 2011; Kopp-Scheinpflug et al., 2011). However, this rebound response could not occur in NL neurons *in vivo* because GABAergic inputs are depolarizing and therefore cannot relieve the inactivation of CaT current in the neurons (Hyson et al., 1995).

Functional relevance of the CaT current in low-CF NL neurons

CaT channels are not expressed in higher-CF neurons but preferentially in low-CF neurons of posthatch animals. This could be advantageous in the scheme of frequency-specific ITD encoding within the NL. NL neurons receive excitatory synaptic inputs from both sides of the nucleus magnocellularis at a rate similar to their CF (Slee et al., 2010; Funabiki et al., 2011; Ashida et al., 2013). Accordingly, the rate of inputs becomes high, and temporal summation of EPSPs becomes large for high-CF neurons (~3 kHz), which causes large steady depolarization and decreases EPSP amplitudes at individual phases in the neurons. This implies that the difference in the peak voltage responses becomes small between in-phase and out-of-phase inputs in the high-CF neurons, which may activate CaT channels regardless of ITDs. In contrast, the

rate of inputs is low, and therefore, in-phase and out-of-phase inputs may still cause a large difference in the peak voltage responses in the low-CF neurons (~0.5 kHz), allowing CaT channels to activate preferentially at the in-phase inputs.

Importantly, the CaT current had little effect on the time course of EPSPs (Fig. 6), because the LVA K⁺ current was activated during the EPSPs and suppressed their prolongation via the CaT current. In addition, the low-CF NL neurons receive strong GABAergic inputs (Nishino et al., 2008; Yamada et al., 2013), which may further counterbalance the effects of the CaT current during the EPSPs. Thus, the effects of the CaT current on the EPSP time course would be minimized in the low-CF neurons. The CaT current not only boosted EPSPs at dendrites but also augmented spike bursts at the AIS. This effect of the CaT current at the AIS could be more prominent in the low-CF neurons than in higher-CF neurons because the AIS is located much closer to the soma in these neurons (Kuba et al., 2006), and the CaT current would be activated more efficiently via synaptic depolarization. Thus, CaT channels are strategically expressed along the tonotopic axis within the NL, which could contribute to ITD detection for a wide range of sound frequencies in the nucleus.

References

Ashida G, Funabiki K, Carr CE (2013) Theoretical foundations of the sound analog membrane potential that underlies coincidence detection in the barn owl. Front Comput Neurosci 7:151. CrossRef Medline

Bender KJ, Trussell LO (2009) Axon initial segment Ca²⁺ channels influence action potential generation and timing. Neuron 61:259–271. CrossRef Medline

Blackmer T, Kuo SP, Bender KJ, Apostolides PF, Trussell LO (2009) Dendritic calcium channels and their activation by synaptic signals in auditory coincidence detector neurons. J Neurophysiol 102:1218–1226. CrossRef Medline

Brown AD, Stecker GC (2010) Temporal weighting of interaural time and level differences in high-rate click trains. J Acoust Soc Am 128:332–341. CrossRef Medline

Cain SM, Snutch TP (2010) Contributions of T-type calcium channel isoforms to neuronal firing. Channels 4:475–482. CrossRef Medline

Casseday JH, Ehrlich D, Covey E (1994) Neural tuning for sound duration: role of inhibitory mechanisms in the inferior colliculus. Science 264:847–850. CrossRef Medline

Chameau P, Lucas P, Melliti K, Bournaud R, Shimahara T (1999) Development of multiple calcium channel types in cultured mouse hippocampal neurons. Neuroscience 90:383–388. CrossRef Medline

Chemin J, Monteil A, Perez-Reyes E, Bourinet E, Nargeot J, Lory P (2002) Specific contribution of human T-type calcium channel isotypes (α₁G, α₁H and α₁I) to neuronal excitability. J Physiol 540:3–14. CrossRef Medline

Christie BR, Eliot LS, Ito K, Miyakawa H, Johnston D (1995) Different Ca²⁺ channels in soma and dendrites of hippocampal pyramidal neurons mediate spike-induced Ca²⁺ influx. J Neurophysiol 73:2553–2557. Medline

Coulter DA, Huguenard JR, Prince DA (1989) Calcium currents in rat thalamocortical relay neurones: kinetic properties of the transient, low-threshold current. J Physiol 414:587–604. CrossRef Medline

Diedesch AC, Stecker GC (2015) Temporal weighting of binaural information at low frequencies: discrimination of dynamic interaural time and level differences. J Acoust Soc Am 138:125–133. CrossRef Medline

Evans MD, Sammons RP, Lebron S, Dumitrescu AS, Watkins TB, Uebele VN, Renger JJ, Grubb MS (2013) Calcineurin signaling mediates activity-dependent relocation of the axon initial segment. J Neurosci 33:6950–6963. CrossRef Medline

Faure PA, Fremouw T, Casseday JH, Covey E (2003) Temporal masking reveals properties of sound-evoked inhibition in duration-tuned neurons of the inferior colliculus. J Neurosci 23:3052–3065. Medline

Felix RA 2nd, Fridberger A, Leijon S, Berrebi AS, Magnusson AK (2011) Sound rhythms are encoded by postinhibitory rebound spiking in the superior paraolivary nucleus. J Neurosci 31:12566–12578. CrossRef Medline

Funabiki K, Ashida G, Konishi M (2011) Computation of interaural time difference in the owl's coincidence detector neurons. J Neurosci 31:15245–15256. CrossRef Medline

Gillessen T, Alzheimer C (1997) Amplification of EPSPs by low Ni^{2+}- and amiloride-sensitive Ca^{2+} channels in apical dendrites of rat CA1 pyramidal neurons. J Neurophysiol 77:1639–1643. Medline

Huguenard JR (1996) Low-threshold calcium currents in central nervous system neurons. Annu Rev Physiol 58:329–348. CrossRef Medline

Hyson RL, Reyes AD, Rubel EW (1995) A depolarizing inhibitory response to GABA in brainstem auditory neurons of the chick. Brain Res 677:117–126. CrossRef Medline

Köppl C, Carr CE (2008) Maps of interaural time difference in the chicken's brainstem nucleus laminaris. Biol Cybern 98:541–559. CrossRef Medline

Kopp-Scheinpflug C, Tozer AJ, Robinson SW, Tempel BL, Hennig MH, Forsythe ID (2011) The sound of silence: ionic mechanisms encoding sound termination. Neuron 71:911–925. CrossRef Medline

Kuba H (2007) Cellular and molecular mechanisms of avian auditory coincidence detection. Neurosci Res 59:370–376. CrossRef Medline

Kuba H, Yamada R, Ohmori H (2003) Evaluation of the limiting acuity of coincidence detection in nucleus laminaris of the chicken. J Physiol 552:611–620. CrossRef Medline

Kuba H, Yamada R, Fukui I, Ohmori H (2005) Tonotopic specialization of auditory coincidence detection in nucleus laminaris of the chick. J Neurosci 25:1924–1934. CrossRef Medline

Kuba H, Ishii TM, Ohmori H (2006) Axonal site of spike initiation enhances auditory coincidence detection. Nature 444:1069–1072. CrossRef Medline

Kuba H, Adachi R, Ohmori H (2014) Activity-dependent and activity-independent development of the axon initial segment. J Neurosci 34:3443–3453. CrossRef Medline

Levic S, Dulon D (2012) The temporal characteristics of Ca^{2+} entry through L-type and T-type Ca^{2+} channels shape exocytosis efficiency in chick auditory hair cells during development. J Neurophysiol 108:3116–3123. CrossRef Medline

Magee JC, Carruth M (1999) Dendritic voltage-gated ion channels regulate the action potential firing mode of hippocampal CA1 pyramidal neurons. J Neurophysiol 82:1895–1901. Medline

Magee JC, Johnston D (1995) Synaptic activation of voltage-gated channels in the dendrites of hippocampal pyramidal neurons. Science 268:301–304. CrossRef Medline

Martin-Caraballo M, Greer JJ (2001) Voltage-sensitive calcium currents and their role in regulating phrenic motoneuron electrical excitability during the perinatal period. J Neurobiol 46:231–248. CrossRef Medline

Mouginot D, Bossu JL, Gähwiler BH (1997) Low-threshold Ca^{2+} currents in dendritic recordings from Purkinje cells in rat cerebellar slice cultures. J Neurosci 17:160–170. Medline

Nishino E, Yamada R, Kuba H, Hioki H, Furuta T, Kaneko T, Ohmori H (2008) Sound-intensity-dependent compensation for the small interaural time difference cue for sound source localization. J Neurosci 28:7153–7164. CrossRef Medline

Parks TN, Collins P, Conlee JW (1983) Morphology and origin of axonal endings in nucleus laminaris of the chicken. J Comp Neurol 214:32–42. CrossRef Medline

Perez-Reyes E (2003) Molecular physiology of low-voltage-activated T-type calcium channels. Physiol Rev 83:117–161. CrossRef Medline

Rubel EW, Parks TN (1975) Organization and development of brain stem auditory nuclei of the chicken: tonotopic organization of *N. magnocellularis* and *N. laminaris*. J Comp Neurol 164:411–433. CrossRef Medline

Shipe WD, Barrow JC, Yang ZQ, Lindsley CW, Yang FV, Schlegel KA, Shu Y, Rittle KE, Bock MG, Hartman GD, Tang C, Ballard JE, Kuo Y, Adarayan ED, Prueksaritanont T, Zrada MM, Uebele VN, Nuss CE, Connolly TM, Doran SM, et al. (2008) Design, synthesis, and evaluation of a novel 4-aminomethyl-4-fluoropiperidine as a T-type Ca^{2+} channel antagonist. J Med Chem 51:3692–3695. CrossRef Medline

Slee SJ, Higgs MH, Fairhall AL, Spain WJ (2010) Tonotopic tuning in a sound localization circuit. J Neurophysiol 103:2857–2875. CrossRef Medline

Smith DJ, Rubel EW (1979) Organization and development of brain stem auditory nuclei of the chicken: dendritic gradients in nucleus laminaris. J Comp Neurol 186:213–239. CrossRef Medline

Talbot MJ, Sayer RJ (1996) Intracellular QX-314 inhibits calcium currents in hippocampal CA1 pyramidal neurons. J Neurophysiol 76:2120–2124. Medline

Uebachs M, Schaub C, Perez-Reyes E, Beck H (2006) T-type Ca^{2+} channels encode prior neuronal activity as modulated recovery rates. J Physiol 571:519–536. CrossRef Medline

Yamada R, Kuba H, Ishii TM, Ohmori H (2005) Hyperpolarization-activated cyclic nucleotide-gated cation channels regulate auditory coincidence detection in nucleus laminaris of the chick. J Neurosci 25:8867–8877. CrossRef Medline

Yamada R, Okuda H, Kuba H, Nishino E, Ishii TM, Ohmori H (2013) The cooperation of sustained and phasic inhibitions increases the contrast of ITD-tuning in low-frequency neurons of the chick nucleus laminaris. J Neurosci 33:3927–3938. CrossRef Medline

Yasuda R, Nimchinsky EA, Scheuss V, Pologruto TA, Oertner TG, Sabatini BL, Svoboda K (2004) Imaging calcium concentration dynamics in small neuronal compartments. Sci STKE 2004:pl5. CrossRef Medline